Numerical Solutions to the Schrödinger Equation

Jake Libbeter, James Freeman, Toby Brown, Thomas Bickley.

Department of Physics: PHYS305
University of Liverpool

Project title: **PHYS305 Numerical solutions to the Schrodinger Equation**
Directory of .ipynb notebook: **main.ipynb**

Abstract

Quantum physics is a branch of physics that explores the behaviour of subatomic particles on scales far removed from everyday experience. By modelling the dynamics of quantum particles in both time-independent and time-dependent potentials, it is possible to develop a deeper understanding of otherwise complex and unintuitive phenomena. This project applies two numerical methods, being the finite difference method for solving the time-independent Schrödinger equation, and the Crank–Nicolson scheme for the time-dependent case. An accompanying animation tool was developed to visualise wavefunction evolution in real time, offering intuitive insight into the underlying mechanics such as quantum tunnelling. An extension to the original aims involved computing the radial eigenfunctions of the hydrogen atom for a given orbital angular momentum value ℓ. The project was highly successful, with each component producing results in close agreement with analytical expectations. Minor limitations were identified, including artificial reflection at the simulation boundaries due to the absence of absorbing boundary conditions. Suggested future improvements include the implementation of time-dependent potentials and the extension of the hydrogen model to incorporate angular components, enabling reconstruction of the full three-dimensional wavefunction.

Contents

1 Motivation (Jake)

Since Schrödinger first introduced his wave equation in 1926 [1], physicists have struggled to find reliable ways to predict quantum behaviour when analytic solutions simply do not exist. Initially, the finite-difference approach offered a natural bridge by replacing continuous derivatives with discrete differences on a spatial grid. The complex partial differential equation collapses into a more manageable set of linear algebraic equations [2]. Although easy to implement, explicit finite-difference methods come with a big downside: their stability requirements force you to use very tiny time steps, so running simulations over long periods can become computationally expensive.

To address these limitations, researchers turned to a method first proposed in the late 1940s, the Crank–Nicolson method [3]. Rather than relying solely on the current time step, it takes an average of the spatial discretisation at both the current and the next time step. This yields second-order accuracy in space and time and is unconditionally stable, allowing much larger time steps without sacrificing reliability. Importantly, for quantum simulations, the scheme exactly conserves the wave function norm, preventing any artificial gain or loss of probability during long evolutions. As a result, the finite-difference Crank–Nicolson approach has become the standard tool for modelling wave-packet dynamics, tunnelling processes, and bound state spectra in one to three dimensional systems.

Taking notes from the student paper Numerical resolution of the Schrödinger equation [4], we adopt its finite-difference grid setup and norm-conserving Crank–Nicolson approach to produce simulations that are both unconditionally stable, and second order accurate.

An example application of these methods is to simulate a double-well potential, which underlies ammonia-inversion spectroscopy [5], where the tunnelling of the nitrogen atom between two wells produces the characteristic inversion spectrum.

2 Background Physics (Jake, James)

The development of quantum mechanics represents one of the most significant advances in the history of physics. During the late nineteenth century, the field experienced rapid progress, marked by the successful formulation of thermodynamic principles and Faraday's discovery of electromagnetic induction. These achievements played a pivotal role in driving the Industrial Revolution and reshaping both scientific understanding and technological capability [6].

James Clerk Maxwell's development of the theory of electromagnetism, which unites electricity, magnetism, and light within a single framework, marked a major breakthrough in nineteenth-century physics. In demonstrating that light behaves as an electromagnetic wave, Maxwell fundamentally changed the scientific understanding of optical phenomena [7].

With these foundations established, physicists turned their attention to a puzzling problem: the behaviour of heated objects and the colours they emit at different temperatures. Attempts to explain this using classical thermodynamics and Maxwell's equations led to the Rayleigh-Jeans law [8]:

$$I(\lambda, T) = \frac{2ck_BT}{\lambda^4} \ , \tag{1}$$

where $I(\lambda, T)$ is the spectral radiance, c is the speed of light, k_B is Boltzmann's constant, T is the absolute temperature, and λ is the wavelength.

While this model matched experimental results at long wavelengths, it incorrectly predicted an unphysical divergence at short wavelengths, implying that heated objects should emit infinite energy. This clear failure became known as the ultraviolet catastrophe.

In December 1900, Max Planck proposed a radical solution: energy could only be emitted or absorbed in discrete packets, or quanta, of size:

$$E = nhf \ , \tag{2}$$

where E is the energy, n is an integer, h is Planck's constant, and f is the frequency of radiation. Using this assumption, Planck derived the Planck radiation law [9]:

$$I(\lambda, T) = \frac{2hc^2}{\lambda^5} \frac{1}{e^{\frac{hc}{\lambda k_B T}} - 1} \ , \tag{3}$$

which agreed with experimental observations across all wavelengths and successfully resolved the ultraviolet catastrophe.

Planck's hypothesis of energy quantisation laid the groundwork for further developments. In particular, in 1905, Albert Einstein extended this idea to explain the photoelectric effect. He proposed that light itself consists of discrete packets, or photons, each carrying energy [10]:

$$E = hf \ , \tag{4}$$

where f is the frequency of the light. Einstein's model accounted for experimental findings which showed that electrons are emitted from a metal surface only if the incident light exceeds a certain frequency threshold, regardless of its intensity. This provided strong evidence for the particle-like nature of light.

In 1913, Niels Bohr further extended the concept of quantisation to atomic structure. He proposed that electrons orbit the nucleus in discrete, stable orbits with angular momentum, L, given by [11]:

$$L = n\hbar \ , \tag{5}$$

where $\hbar = \frac{h}{2\pi}$ is the reduced Planck's constant. Bohr's model successfully explained the observed spectral lines of hydrogen. However, it was later shown to be inadequate for multi-electron atoms and incor-

rectly predicted the ground-state angular momentum of the hydrogen atom to be $\hbar$, whereas experiments revealed it to be zero.

By 1925, new ideas were emerging to address these limitations. Louis de Broglie proposed that if light, traditionally understood as a wave, could exhibit particle-like properties, then particles such as electrons might also exhibit wave-like behaviour. He suggested that the wavelength associated with a particle is given by [12]:

$$\lambda = \frac{h}{p} \ , \tag{6}$$

where p is the particle's momentum.

Inspired by de Broglie's hypothesis, Erwin Schrödinger formulated a wave equation to describe the dynamics of quantum systems. The time-dependent Schrödinger equation is given by [13]:

$$i\hbar \frac{\partial \psi_n(\vec{r}, t)}{\partial t} = \hat{H}\psi_n(\vec{r}, t) \ , \tag{7}$$

where $\psi_n(\vec{r}, t)$ is the wavefunction corresponding to the n^{th} excited state, and $\hat{H}$ is the Hamiltonian operator representing the total energy of the system, which is defined as:

$$\hat{H} = -\frac{\hbar^2}{2m}\nabla^2 + V(\vec{r}, t) \ , \tag{8}$$

with $\nabla^2 = \frac{\partial^2}{\partial x^2} + \frac{\partial^2}{\partial y^2} + \frac{\partial^2}{\partial z^2}$. For a one-dimensional potential that does not depend on time, it can be postulated that: $\psi(x, t) = \psi(x)e^{-iE_n t/\hbar}$, where E_n is the energy of the n^{th} state. In this case, the time-dependent Schrödinger equation reduces to the time-independent form:

$$E_n\psi_n(x) = \hat{H}\psi_n(x) \ , \tag{9}$$

which governs the stationary states of the system.

The solutions to both the time-dependent and time-independent Schrödinger equations vary depending on the potential to which the particle is subjected. In physics, a range of model potentials are commonly employed to represent different physical systems. The complexity of solving the Schrödinger equation depends heavily on the form of the potential, with only a limited number of cases admitting exact, analytical solutions.

This project focuses on a selection of standard potentials for which analytic solutions are known, including the free particle, the infinite potential well (IPW), the finite potential well (FPW), the harmonic oscillator (HO), and the Coulomb potential, all of which will be discussed in detail later in the report.

The primary aim of this project is to numerically solve the time-independent Schrödinger equation for a range of potentials with known analytic solutions using the finite difference method. The numerical results obtained will then be compared against the exact solutions in order to assess the accuracy and reliability of the finite difference approach.

In addition to these studies, more complex potentials, such as the double-well potential, will also be examined. Furthermore, the time-dependent Schrödinger equation will be solved using the Crank–Nicolson method. By simulating the evolution of wave packets, the transmission and reflection coefficients across various potential barriers will be calculated, thereby allowing for a detailed investigation of quantum tunnelling phenomena under different conditions.

.

3 Introduction

3.1 Finite Difference Method (Jake and James)

The finite difference (FD) method is a numerical approach used to solve differential equations by discretising the continuous problem. It converts differential equations into systems of algebraic equations, which can then be solved numerically to approximate the original solutions [14]. The FD method is widely employed in mathematics and physics to model real-world phenomena. For instance, it can be applied to thermodynamic problems by solving the heat equation [15], or to quantum mechanical systems where analytical solutions are difficult to obtain.

One of the strengths of the FD method lies in its ability to accommodate complex boundary conditions and arbitrary potential profiles. It achieves high accuracy in approximating second-order derivatives through the use of a uniform computational grid, ensuring reliable results, particularly for smooth potential functions.

To begin solving the time-independent Schrödinger equation using the finite difference method, the spatial domain $[a, b]$ is discretised into N equally spaced points, where the grid spacing is defined as $\Delta x = \frac{b-a}{N}$ and the grid points are given by $x_i = a + i\Delta x$, where i ranges from 1 to N. The wavefunction $\psi(x)$ is approximated at these discrete points as $\psi_i = \psi(x_i)$, where the wavefunctions form an orthonormal set, defined by:

$$\langle \psi_n | \psi_m \rangle = \delta_{nm} = \begin{cases} 0, & n \neq m \\ 1, & n = m \end{cases} . \tag{10}$$

Next, the second-order derivative can be approximated using the finite difference formula [16]:

$$\frac{d^2\psi(x)}{dx^2} \approx \frac{\psi_{i+1} - 2\psi_i + \psi_{i-1}}{\Delta x^2} , \tag{11}$$

Substituting this approximation into **Eqn. 9** yields:

$$-\frac{\hbar^2}{2m}\frac{\psi_{i+1}-2\psi_i+\psi_{i-1}}{\Delta x^2}+V_i\psi_i=E\psi_i\ , \tag{12}$$

which can be rearranged into the form:

$$-\alpha\psi_{i+1}+(2\alpha+V_i)\psi_i-\alpha\psi_{i-1}=E\psi_i\ , \tag{13}$$

where $\alpha=\frac{\hbar^2}{2m\Delta x^2}$.

The Hamiltonian matrix corresponding to this discretisation is given by:

$$\mathbf{H}=\begin{bmatrix} 2\alpha+V_1 & -\alpha & 0 & \cdots & 0 \\ -\alpha & 2\alpha+V_2 & -\alpha & \cdots & 0 \\ 0 & -\alpha & 2\alpha+V_3 & \cdots & 0 \\ \vdots & \vdots & \vdots & \ddots & \vdots \\ 0 & 0 & 0 & \cdots & 2\alpha+V_N \end{bmatrix}\ , \tag{14}$$

and the resulting eigenvalue problem can be expressed in matrix form as:

$$\mathbf{H}\vec{\psi}=E\vec{\psi}\ , \tag{15}$$

where $\vec{\psi}$ is the vector of wavefunction values at the grid points.

In many physical systems, the resulting matrices are sparse and banded, meaning that nonzero entries are confined near the diagonal. This structure allows for significant improvements in computational efficiency when specialised numerical techniques are employed, such as those taking advantage of the banded form.

Here, the energy eigenvalues and eigenvectors are defined at discrete points on the computational grid. To solve the resulting eigenvalue problem, the function `eigh_tridiagonal` from the `scipy.linalg` module can be employed. This function computes the eigenvalues and eigenvectors of a symmetric tridiagonal matrix efficiently [17].

The Hamiltonian matrix presented in **Eqn. 14** has diagonal elements given by $2\alpha + V_i$ and constant off-diagonal elements equal to $-\alpha$. Rather than constructing the full matrix explicitly, the SciPy module `eigh_tridiagonal` exploits the tridiagonal structure and applies iterative algorithms such as the Lanczos method [18]. The Lanczos method generates a sequence of orthonormal vectors and eigenvalue approximations, which converge towards the true eigenvalues and eigenvectors as the number of iterations increases.

Additionally, the QR algorithm is employed to further refine the computed eigenvalues and eigenvectors. By taking advantage of the sparse, symmetric nature of the Hamiltonian, `eigh_tridiagonal` significantly

reduces both memory requirements and computational cost compared to standard methods designed for dense matrices.

3.2 Crank-Nicolson Method (Jake)

The next step is the introduction of a numerical approach to solve the time-dependent Schrödinger equation. In this project, the Crank-Nicolson method [3] is used due to its numerical stability and norm conservation properties, as identified in prior student work.

The Crank-Nicolson method, first proposed by John Crank and Phyllis Nicolson in 1947, provides a reliable technique for obtaining numerical solutions to differential equations. One of its key advantages is its convergence and unconditional stability for all finite values of the stability parameter λ. In particular, the method remains stable even for large values of λ, where stability is maintained provided $\frac{\Delta t}{\Delta x^2} < \lambda$ [19]. This feature is essential in the present work, allowing for accurate and reliable results that are independent of time step and spatial grid resolution.

The time-dependent Schrödinger equation, expressed in terms of the Hamiltonian operator $\hat{H}$, is given in **Eqn. 7**. Following a similar approach to the finite difference method, the wavefunction $\psi(x,t)$ is discretised over a spatial grid, whilst time is divided into discrete intervals t_n with uniform spacing Δt.

To solve the time-dependent Schrödinger equation using the Crank-Nicolson method, a centred difference scheme is applied to approximate the time derivative. This approach averages the time evolution between two successive time intervals, t_n and t_{n+1}, thereby improving the accuracy and stability of the numerical solution.

$$\left.\frac{\psi^{n+1}-\psi^{n}}{\Delta t}\right|_{t_{n+\frac{1}{2}}} = -\frac{i}{\hbar}\left.\left(\frac{\hat{H}\psi^{n+1}+\hat{H}\psi^{n}}{2}\right)\right|_{t_{n+\frac{1}{2}}} . \tag{16}$$

The average of the time evolution can be rearranged as:

$$\left(I-\frac{i\Delta t}{2\hbar}\hat{H}\right)\psi^{n+1} = \left(I+\frac{i\Delta t}{2\hbar}\hat{H}\right)\psi^{n} , \tag{17}$$

where I is the identity matrix. **Eqn. 17** can be written in matrix form as:

$$A\psi^{n+1} = B\psi^{n} , \tag{18}$$

where $A = \left(I-\frac{i\Delta t}{2\hbar}\hat{H}\right)$ and $B = \left(I+\frac{i\Delta t}{2\hbar}\hat{H}\right)$, with the Hamiltonian operator defined as in the finite difference section. This formulation allows the wavefunction at the next time step to be obtained directly from the previous time step.

Thus, ψ^{n+1} can be formally written as:

$$\psi^{n+1} = A^{-1}B\psi^n \ . \tag{19}$$

However, solving this analytically is generally intractable for non-trivial systems, and thus numerical techniques are required.

3.3 Solutions for Different Potentials (Tom, James)

In order to compute the Hamiltonian matrix, the potential, $V(x)$, must be defined and calculated at every point in space. As discussed previously, the potentials that are studied in this project are the infinite potential well, finite potential well, the harmonic oscillator, the coulomb potential and a double potential well. This section will outline the steps that is analytically used to solve the time independent Schrödinger equation for an infinite potential well. From this, an analytical expression for the energy levels will be obtained. In addition, the eigenstates and energy eigenvalues to the time independent Schrödinger equation will be given for the finite potential well, harmonic oscillator and coulomb potential. This will allow for a direct comparison of the analytical solutions with the numerical solutions obtained through the finite difference method.

3.3.1 Infinite Potential Well (IPW)

$$V(x) = \begin{cases} 0, & x_{\min} \leq x \leq x_{\max} \\ \infty, & \text{otherwise} \end{cases} \ . \tag{20}$$

The time-independent Schrödinger equation for an infinite potential well between $x_{\min} \leq x \leq x_{\max}$ can be rearranged as such:

$$\frac{d^2\psi(x)}{dx^2} + \frac{2m}{\hbar^2}E\psi(x) = 0 \ . \tag{21}$$

The solution is the sum of the two plane waves propagating in opposite directions, which is equivalent to the sum of a cosine and a sine (i.e., standing waves), with wave number k. The general solution is of the form [20]:

$$\psi(x) = A'e^{ikx} + B'e^{-ikx} = A\cos(kx) + B\sin(kx) \ , \tag{22}$$

where the wave number is given by:

$$k = \sqrt{\frac{2mE}{\hbar^2}} \ . \tag{23}$$

To find the complete solution, boundary conditions must be imposed. At x = a and x = -a the wavefunction must be zero.

$$A\cos(ka) + B\sin(ka) = 0 \ , \tag{24}$$

$$A\cos(ka) - B\sin(ka) = 0 \ , \tag{25}$$

Solving these equations gives:

$$A\cos(ka) = 0 \quad \text{and} \quad B\sin(ka) = 0 \ . \tag{26}$$

For the above condition to be true, the wave number must be quantised as shown below:

$$\cos(ka) = 0 \Rightarrow k_n = \frac{n\pi}{2a} = \frac{n\pi}{L}, \quad n = 1, 3, 5, \dots \ . \tag{27}$$

$$\sin(ka) = 0 \Rightarrow k_n = \frac{n\pi}{2a} = \frac{n\pi}{L}, \quad n = 2, 4, 6, \dots \ . \tag{28}$$

This condition leads to even and odd parity solutions. The next step is to obtaining a complete solution is to apply the normalisation condition:

$$\int_{-a}^{a} \psi_n^*(x)\psi_n(x) \ dx = 1 \ . \tag{29}$$

For example, considering the cosine solution:

$$\int_{-a}^{a} A^2\cos^2(kx) \ dx = A^2\frac{1}{2}(a - (-a)) = A^2 a = 1 \ . \tag{30}$$

Solving for A:

$$A = \frac{1}{\sqrt{a}} \ . \tag{31}$$

The solutions can now be summarised by even or odd parity solutions depending on the value of the quantum number n. Even parity solutions are solutions with even functions, $\psi_n(x) = \psi_n(-x)$ and odd parity solutions are solutions with odd functions, $\psi_n(-x) = -\psi_n(x)$.

Even parity:

$$\psi_n(x) = \frac{1}{\sqrt{a}}\cos\left(\frac{n\pi}{2a}x\right), \quad n = 1, 3, 5, \dots \ . \tag{32}$$

Odd parity:

$$\psi_n(x) = \frac{1}{\sqrt{a}}\sin\left(\frac{n\pi}{2a}x\right), \quad n = 2, 4, 6, \dots \ . \tag{33}$$

The de Broglie wavelength can now be evaluated:

$$k_n = \frac{n\pi}{2a} \Rightarrow \lambda_n = \frac{2\pi}{k_n} = \frac{2L}{n}, \quad n = 1, 2, 3, 4, \dots \ . \tag{34}$$

This result shows that only half-integer and integer wavelengths fit in the box.

The final step is to determine the energy of each level in the box. Since the wave number is quantised, it follows that the energy eigenvalues must also be quantised.

$$E_n = \frac{p^2}{2m} = \frac{\hbar^2 k_n^2}{2m} = \frac{\hbar^2 \pi^2 n^2}{2ma^2} = \frac{h^2 n^2}{8ma^2} \ . \tag{35}$$

3.3.2 Finite Potential Well

The finite potential is defined such that there is no potential inside the well and a constant potential, V_0, outside the well. This can be mathematically described as such:

$$V(x) = \begin{cases} 0, & -a \leq x \leq a \\ V_0, & \text{otherwise} \end{cases} \ . \tag{36}$$

A key difference between the infinite and finite potential wells is that, since there is a constant potential outside the well, the wavefunction can not be zero. By taking a similar approach shown for the infinite potential well and also imposing continuity of the wavefunction at the boundary, even and odd parity solutions for the time independent Schrödinger equation can be obtained inside and outside the well.

Odd parity:

$$\psi(x) = \begin{cases} -Ce^{+\kappa x} & x \leq -a \\ A\sin(qx) & |x| \leq a \\ Ce^{-\kappa x} & x \geq +a \end{cases} \ . \tag{37}$$

Even parity:

$$\psi(x) = \begin{cases} Ce^{+\kappa x} & x \leq -a \\ B\cos(qx) & |x| \leq a \\ Ce^{-\kappa x} & x \geq +a \end{cases} \ . \tag{38}$$

with $q = \sqrt{2mE}/\hbar$ and $\kappa = \sqrt{2m(V_0 - E)}/\hbar$ [21].

3.3.3 Double Potential Well

$$V(x) = \begin{cases} 0, & x_{\min,1} \leq x \leq x_{\max,1} \text{ or } x_{\min,2} \leq x \leq x_{\max,2} \\ V_{1,2}, & \text{otherwise} \end{cases} \ , \tag{39}$$

in which, subscripts 1,2 represent each individual well in the system [22].

The double potential well is an extension of the finite potential well. The physical concepts remain the same, however, the mathematics is considerably more challenging to find approximate solutions analytically. As a result, the finite difference method is a very powerful tool here since it can find an approximate solution for these types of problems.

3.3.4 Harmonic Oscillator

The harmonic oscillator potential is defined as [23]:

$$V(x) = \frac{1}{2}m\omega^2 x^2 \ , \tag{40}$$

where ω is the angular frequency of the particle that is subject to the potential. This potential leads to the time independent Schrödinger equation of the form

$$-\frac{\hbar^2}{2m}\frac{d^2\psi}{dx^2} + \frac{1}{2}m\omega^2 x^2\psi = E\psi \ . \tag{41}$$

It can be shown that the solutions take the form: [24]:

$$\psi_n(x) = A_n H_n(\zeta x)\exp\left(\frac{-\zeta^2 x^2}{2}\right) , \tag{42}$$

where A_n is a normalisation constant and $H_n(\zeta x)$ refers to the Hermite polynomials with $\zeta = \sqrt{\frac{m\omega}{\hbar}}$. It can also be shown that this solution leads to energy eigenvalues of:

$$E_n = \left(n + \frac{1}{2}\right)\hbar\omega. \tag{43}$$

3.3.5 Central potential

A common potential used throughout physics is a central potential, $V(\vec{r})$. A cemtral potential is a potential that is only dependent on the particles distance from the origin. To solve the Schrödinger equation for a central potential, it proves useful to use 3D spherical coordinates. Substituting in the Laplacian operator in spherical coordinates into the time independent Schrödinger equation gives,

$$-\frac{\hbar^2}{2m}\left[\frac{1}{r^2}\frac{\partial}{\partial r}\left(r^2\frac{\partial\psi}{\partial r}\right) + \frac{1}{r^2\sin\theta}\frac{\partial}{\partial\theta}\left(\sin\theta\frac{\partial\psi}{\partial\theta}\right) + \frac{1}{r^2\sin^2\theta}\left(\frac{\partial^2\psi}{\partial\phi^2}\right)\right] + V(\vec{r})\psi = E\psi \ , \tag{44}$$

where $\psi = \psi(\vec{r},\theta,\phi)$, θ is the polar angle, and ϕ is the azimuthal angle. It can be postulated that $\psi(\vec{r},\theta,\phi) = R(\vec{r})Y(\theta,\phi)$. This postulate can be shown to lead to the radial Schrödinger equation,

$$-\frac{\hbar^2}{2m}\frac{d^2u(\vec{r})}{dr^2}+\left(V(\vec{r})+\frac{\hbar^2\ell(\ell+1)}{2mr^2}\right)u(\vec{r})=Eu(\vec{r})\ , \tag{45}$$

where $u(\vec{r})=rR(\vec{r})$ and ℓ is the orbital angular momentum quantum number. The radial Schrödinger equation can take the same form as the regular time-independent Schrödinger equation,

$$-\frac{\hbar^2}{2m}\frac{d^2u(\vec{r})}{dr^2}+V_{\text{eff}}\ u(\vec{r})=Eu(\vec{r})\ , \tag{46}$$

where V_{eff} is the effective potential and is equal to $\left(V(\vec{r})+\frac{\hbar^2\ell(\ell+1)}{2mr^2}\right)$. This form allows the finite difference method to be obtain eigenfunctions and eigenvectors for systems that are subject to a central potential. The eigenfunctions obtained will still give the energy of the system as discrete points in space, however the eigenvectors will give a function for $u(\vec{r})$. Dividing $u(\vec{r})$ by r will lead to the radial solution of the Schrödinger equation for any central potential.

3.3.6 Coulomb Potential

For a hydrogen atom, the Coulomb potential is given by [25],

$$V(r)=-\frac{e^2}{4\pi\varepsilon_0 r}, \tag{47}$$

where e is the elementary charge of the electron, ε_0 is the permittivity of free space and r is the radial distance from the origin of the particle that is subject to the potential. Since the Coulomb potential is an example of a central potential since it is only dependent on the radial position of the electron. When the Coulomb potential is substituted into the radial Schrödinger equation the solution is given by[26]:

$$R_{n,\ell}(r)=\sqrt{\left(\frac{2}{na_0}\right)^3\frac{(n-\ell-1)!}{2n\left[(n+\ell)!\right]^3}}\cdot e^{-r/(na_0)}\cdot\left(\frac{2r}{na_0}\right)^{\ell}\cdot L^{2\ell+1}_{n-\ell-1}\left(\frac{2r}{na_0}\right)\ . \tag{48}$$

Here, n is the principle quantum number, and is a positive integer, a_0 is the Bohr radius and $L^{2\ell+1}_{n-\ell-1}\left(\frac{2r}{na_0}\right)$ are the associated Laguerre polynomials. It can also be shown that solving the radial Schrödinger equation for the hydrogen atom yields energy levels given by:

$$E_n=-\frac{13.6}{n^2}\ \text{eV}\ . \tag{49}$$

3.4 Quantum tunnelling (Toby)

The concept of quantum tunnelling has had a profound impact in a wide range of areas of physics. For example, in nuclear physics, quantum tunnelling is used to explain the concept of alpha decay [27]. In

addition to this, quantum tunnelling is used in semiconductor physics to model the movement of electrons in Schottky diodes which has had a profound impact of current semiconductor technology devices [28]. Quantum tunnelling involves a quantum particle penetrating a potential barrier, which would classically be forbidden [29]. The probabilty for quantum tunneling to occur, Ω, is given by,

$$\Omega = e^{-2W}\sqrt{\frac{2m(V_0 - E)}{\hbar^2}}, \tag{50}$$

where W is the width of the barrier, V_0 is the height of the barrier and E is the kinetic energy of the particle. There are various potential wells that allow for quantum tunnelling to occur, such as the finite potential well and the harmonic oscillator. This project initially investigates quantum tunnelling in the finite potential well, and then progresses to a double potential well. To investigate the effect of quantum tunnelling, reflection (R), barrier (B) and transmission (T) coefficients can be calculated for an incoming wavepacket incident (I) on a finite potential well. The coefficients can be calculated as shown below.

$$I = \int_{-\infty}^{x_0} |\psi(x, t_0)|^2 \, dx, \tag{51}$$

$$R = \int_{-\infty}^{x_0} |\psi(x, t_f)|^2 \, dx, \tag{52}$$

$$T = \int_{x_0+\Delta x_0}^{\infty} |\psi(x, t_f)|^2 \, dx, \tag{53}$$

$$B = \int_{x_0}^{x_0+\Delta x_0} |\psi(x, t_f)|^2 \, dx. \tag{54}$$

where t_0 is the initial time and t_f is the final time occurring in the wavepacket animation. x_0 is the starting position of the potential well and Δx_0 represents the width of the potential barrier. Furthermore, the barrier width and height will also be varied to investigate how the time taken for tunnelling to occur and the probability that tunnelling occurs is affected by the barrier width and height.

4 Method

4.1 Potentials (Toby, James, Tom)

To model the potentials in python, each potential is structured as a sub class of a base class called `Potential`. The initialisation function of the base class defines dimensional properties of each quantum system such as its width, depth, and centre. These attributes are subsequently inherited when the sub classes are defined. In the sub classes, the subroutine `GetPotential()` from the base class is defined. This function evaluates $V(x)$ for a given position, x, or an array of positions which takes advantage of python's vectorised operations instead of relying on huge iterations that would slow the programme down. The reason for using a base class is to ensure the code is reusable as the user only has to define many attributes once. The attributes include dimensional properties such as the well boundaries, well depth and the centre of the well. In addition to this, physical properties of the particle in question such as the

mass and the charge also only need to be defined once. Calling modules such as `GetPotential()` when carrying out numerical computations isn't strictly tied to a single quantum system, allowing for flexibility when implementing the `Hamiltonian` class.

4.2 Finite Difference Method (Jake)

The numerical solution to the Schrödinger equation **Eqn. 7** began by constructing a `Hamiltonian` class. This class was designed to accept an array of spatial data points, divided into N points separated by a uniform spacing Δx, alongside a potential object as input parameters. This enabled the system to correctly solve the eigenvalue problem defined in **Eqn. 14** and to return a one-dimensional array of eigenvalues and a two-dimensional array of the corresponding eigenvectors.

To simplify the implementation and reduce the risk of floating-point errors associated with extremely large or small physical constants, natural units were adopted by setting $\hbar = 1$ and $m = 1$ throughout the calculations. This approach rendered the Hamiltonian dimensionless, significantly improving numerical stability without altering the physical properties of the system.

The choice of N is crucial: selecting too few points can introduce significant numerical errors, whilst excessively large values of N can lead to increased computational cost. As a result, a balance between numerical accuracy and processing time must be carefully maintained.

By utilising the extensive linear algebra capabilities available in SciPy [30], a solution was implemented using the `scipy.linalg` namespace. In particular, the `eigh_tridiagonal()` function was employed to efficiently exploit the tridiagonal structure of the Hamiltonian matrix.

Following the implementation of the finite difference method, the final steps involved validating the results by testing multiple potentials and comparing the numerical solutions against known analytical results. Further investigation was carried out by evaluating the relative difference between the expected and calculated energies for the infinite potential well, in order to assess the suitability of the chosen step size and the range of quantum numbers considered, making use of the formula:

$$\Delta E = \frac{E_{\text{calc}} - E_{\text{exp}}}{E_{\text{exp}}} \cdot 100\% \ . \tag{55}$$

4.3 Crank-Nicolson Method (Jake)

The implementation of the Crank-Nicolson method was divided into two main stages. The first involved coding the Crank-Nicolson scheme itself, whilst the second focused on developing an animation tool to enable the visualisation of the wavefunction evolution, both for analytical purposes and for use in the final presentation.

To implement the Crank-Nicolson scheme, the previously constructed `Hamiltonian` class was utilised. This class was further extended by applying **Eqn. 18**, with the matrices A and B defined appropriately. Rather than directly inverting A to obtain A^{-1}, which would be computationally expensive, the `scipy.linalg` namespace was again employed. Specifically, the `solve_banded()` function was used to

solve equations of the form $A\vec{x} = \vec{b}$, where A is the previously defined matrix and $\vec{b} = B\vec{\psi}$ is the corresponding column vector, taking advantage of the banded nature of the matrix A to reduce computational complexity.

The `solve_banded()` function accepts three parameters: a tuple specifying the number of super- and sub-diagonal entries, the banded form of the matrix A, and the right-hand side vector $\vec{b}$.

To enable the observation of time evolution, an initial Gaussian wave packet was defined. At each subsequent time step, the wavefunction was iteratively updated and appended to an array called `wavefuncHistory`, ensuring that the complete time evolution of the wave packet was accessible for the animation process in the next stage.

Once the time evolution was successfully implemented, an animation tool was developed using the `matplotlib.animation` and `IPython.display` modules. To correctly animate the wave packet evolution, it was important to distinguish between the duration of the resulting clip, T_{dur}, and the simulated physical time, T_{sim}, to ensure that the animation duration corresponds proportionally to the simulated physical time. These quantities are related through the time step ΔT and the chosen frame rate (FPS) by:

$$T_{\text{dur}} = \frac{T_{\text{sim}}}{\text{FPS} \cdot \Delta T} \ , \tag{56}$$

The animation simultaneously displayed the real and imaginary parts of the wavefunction, the probability density $|\psi(x,t)|^2$, and the scaled potential profile on a shared spatial axis. The use of multiple overlaid plots allowed for clear visualisation of both the wavefunction's structure and its interaction with the potential landscape during time evolution.

To validate the implementation of the Crank-Nicolson method, several qualitative and quantitative checks were performed. One of the key advantages of the Crank-Nicolson method is that it is unitary, meaning that if the initial wavefunction is normalised, the integral of $|\psi(x,t)|^2$ over the spatial domain should remain equal to one throughout the entire time evolution. This property was monitored during the animation to confirm that probability was conserved at all time steps.

In addition, the simulation was examined to ensure that it correctly captured the expected dispersion behaviour of a freely propagating wave packet, as would be observed for a free particle.

4.4 Investigating Quantum Tunnelling (Toby, Tom, James)

A finite potential well was implemented using the potentials class. This project aimed to study the impact of two key parameters on the probability of quantum tunnelling occurring. These parameters are the barrier width and barrier height. In order to do this, the time evolution loop is nested within an outer loop that iterates over the desired barrier widths or heights, enabling systematic measurement of tunnelling dependence on these parameters.

Reflection (R), transmission (T), and barrier occupancy (B) are computed by integrating $|\psi(x,t)|^2$ over spatial regions defined in section 3.4 by **Eq. (52** - 54). The probability density $|\psi(x)|^2$ in each spatial re-

gion is computed using Simpson's rule, implemented via `scipy.integrate.simps`. This method provides $\mathcal{O}(h^4)$ accuracy by approximating the integral using quadratic segments:

$$\int_a^b f(x)dx \approx \frac{h}{3}\left[f(x_0) + 4\sum_{\text{odd } j} f(x_j) + 2\sum_{\text{even } j} f(x_j) + f(x_n)\right] \tag{57}$$

where h is the uniform grid spacing.

Compared to the trapezoidal rule ($\mathcal{O}(h^2)$ accuracy with linear segments), Simpson's rule better captures the curvature of the wavefunction's probability density, particularly near the barrier boundaries. This is because Simpsons rule fits parabolas rather than straight lines.

The finite potential well was as a test case to validate the integration method. The wavefunctions behaviour can be visually distinguished within animations. The coefficients were calculated from the final frame of the time evolution to ensure steady-state conditions. The storage of coefficients for each barrier configuration was done via a dictionary keyed by the barrier width/height for post-loop processing. In this test case, the incident coefficient was calculated in the initial frame (t = 0) and the reflection, transmission and barrier coefficients were calculated in the final frame (t = 2 seconds).

4.4.1 Tunnelling Time

A further investigation into quantum tunnelling was also conducted by calculating the tunnelling time. There are various interpretations of tunnelling time. In this project the transmission time, τ_{trans}, was investigated as well as the dwell time, τ_{dwell}. The transmission time is defined as the time taken for the transmission coefficient to rise above 0.01 where as the dwell time represents how much time was spend in the barrier. In order to compute the transmission time, the transmission coefficient, $T(t)$, must be calculated as a function of time,

$$T(t) = \int_{x_{\min}+w}^{\infty} |\psi(x,t)|^2 \, \mathrm{d}x \tag{58}$$

From this, the transmission time can be found by measuring the time taken for $T(t)$ to become greater than 0.01.

In order to calculate the dwell time, the barrier coeffiecent, $B(t)$, must be known as a function of time. This can be calculated by,

$$B(t) = \int_{x_{\min}}^{x_{\min}+w} |\psi(x,t)|^2 \, \mathrm{d}x \tag{59}$$

The dwell time can then be calculated as,

$$\tau_{\text{dwell}} = \int_0^{\infty} B(t) \;\, \mathrm{d}t \,. \tag{60}$$

4.5 Radial Eigenfunctions (Jake)

To extend the implementation to also calculate the eigenfunctions for the radial component of the hydrogen wavefunction, R_{nl}, only minor modifications to the existing `Hamiltonian` class were required. The principal change involved rewriting the potential to account for more than just the Coulomb interaction. As shown in **Eqn. 46**, the effective potential must be employed, which includes a centrifugal term arising from the electron's angular momentum, becoming increasingly dominant as l increases. This centrifugal term introduces a repulsive component at small r, significantly altering both the effective potential landscape and the corresponding eigenfunctions. In particular, the radial eigenfunctions are pushed outward and their nodal structures are modified as l increases.

Furthermore, appropriate boundary conditions were applied to ensure that $u(r) \to 0$ as $r \to 0$, in accordance with the physical behaviour of the hydrogen atom. These seemingly minor adjustments have significant implications for the results obtained, even when the remainder of the code remains otherwise unchanged.

5 Results and Discussion

5.1 Finite Difference Method

5.1.1 Implementation (Jake)

The one-dimensional Hamiltonian was implemented successfully, yielding valid results across all tested potentials, as illustrated in **Figs. 1a, 1b, 1c**. The obtained results are consistent with the expected physical behaviour of quantum systems. For the infinite potential well (IPW), the probability densities are entirely confined within the well boundaries, with no tunnelling into the classically forbidden regions, in agreement with the presence of infinitely high potential barriers. In contrast, the finite potential well (FPW) exhibits probability densities that extend slightly beyond the edges of the well, decaying exponentially as anticipated due to quantum tunnelling into regions where $E < V(x)$. The harmonic oscillator (HO) solutions display probability densities that spread further from the origin as the energy level increases. In all cases, the number of nodes in the wavefunctions increases with energy, as theoretically predicted.

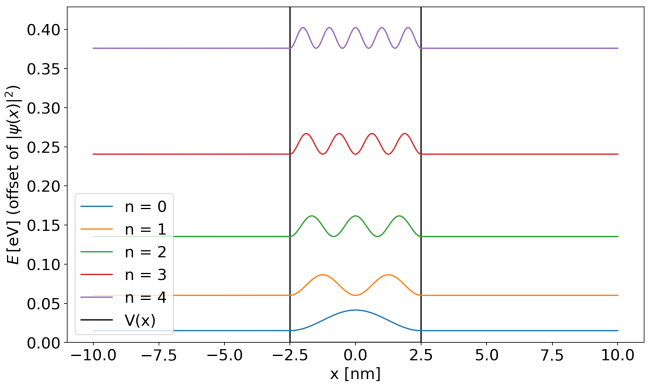

(a) Shows the numerically obtained probability densities $|\psi(x)|^2$ for the infinite potential well for the first five excited states, offset by their eigenvalues in eV, plotted against the distance in nm. The black curve represents the potential $V(x)$ to which the quantum particle is subject, which is equal to zero inside the well and numerically infinite outside the well, and as expected, the wavefunction goes to zero outside the well boundaries.

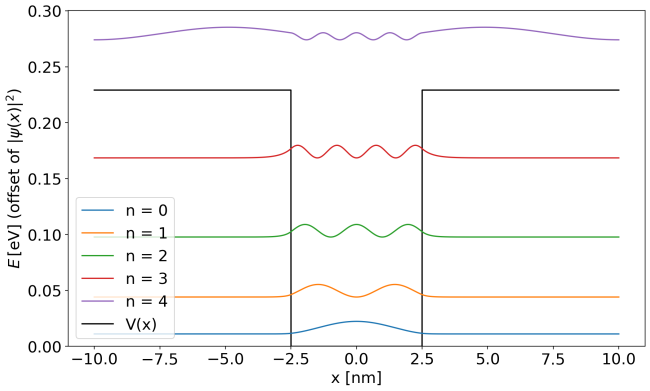

(b) Shows the numerically obtained probability densities $|\psi(x)|^2$ for the finite potential well for the first five eigenstates, offset by their eigenvalues in eV, plotted against the distance in nm. The black curve represents the potential $V(x)$ to which the quantum particle is subject, set to be zero inside the well and given the dimensionless value of 3 outside the well, corresponding to approximately 0.23 eV. Owing to the finite height of the potential barriers, the wavefunctions exhibit exponential decay into the classically forbidden region outside the well boundaries. For $n = 5$, the energy lies above the potential barrier V_0, and the particle occupies a scattering state.

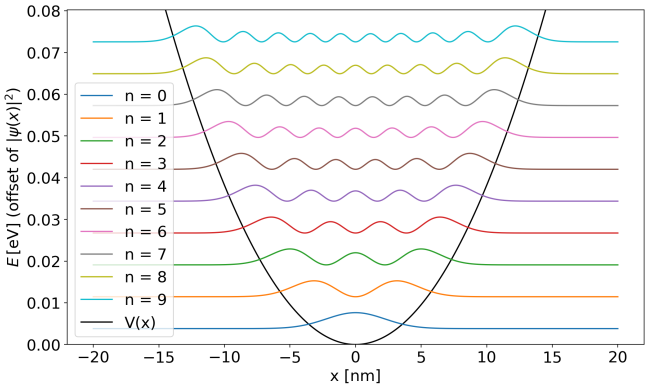

(c) Shows the numerically obtained probability densities $|\psi(x)|^2$ for the harmonic oscillator for the first ten eigenstates, offset by their eigenvalues in eV, plotted against the distance in nm. The black curve represents the parabolic potential $V(x)$ to which the quantum particle is subject, set to have $\omega = 0.1$ in dimensionless units, however this converts to a value of $\omega \approx 1.2 \times 10^{13}$ rad $\cdot\, \mathrm{s}^{-1}$. As expected from the analytical solutions to the quantum harmonic oscillator, the number of nodes increases with each energy level.

Figure 1: Shows the numerically obtained probability densities $|\psi(x)|^2$ for different quantum systems: (a) infinite potential well, (b) finite potential well, and (c) harmonic oscillator. In all cases, the number of spatial data points was set to be $N = 5000$. The amplitude of each $|\psi(x)|^2$ has been scaled arbitrarily for visual clarity.

5.1.2 Ensuring Eigenstates Form an Orthonormal Set (Jake)

To verify that the determined wavefunctions form an orthonormal set, it was necessary to confirm the condition expressed in **Eqn. 10**, and was decided to be tested for the IPW seen in **Fig. 1a**. Since the wavefunctions were manually normalised during the implementation, there was no requirement to revalidate their individual normalisation. However, to ensure the orthogonality between distinct eigenstates, the `scipy.integrate.simps()` method was employed to numerically evaluate the orthogonality integrals.

The mean value obtained for the overlap between two different wavefunctions was found to be $(-2 \pm 5) \times 10^{-12}$, which is clearly consistent with zero at the 3σ confidence level.

This result, combined with the qualitative agreement of the numerically determined wavefunctions with known analytical solutions, provides strong evidence that the finite difference method was correctly implemented.

5.1.3 Investigating the Infinite Potential Well (Jake)

The relative energy error between the expected energy E_{exp} and the numerically calculated energy E_{calc} was investigated as a function of both the principal quantum number n and the number of spatial data points N, by making use of **Eqn. 55**.

When varying n, a polynomial relationship of the form $y = ax^2 + bx + c$ was found, with $a = 9.53 \times 10^{-5}$, $b = 5.25 \times 10^{-7}$, and $c = 0.495$, obtained using `np.polyfit()`. This expression suggests that changes in n lead to only minor variations in the relative difference, with the differences remaining of order 10^{-2} between data points, as illustrated in **Fig. 2a**. This analysis remains included to verify that the choice of n has negligible effect on the relative difference.

In stark contrast, the relative difference is highly sensitive to the number of spatial data points N. As shown in **Fig. 2b**, the value of N plays a crucial role in determining the accuracy of the calculated energies. A power law, of the form $y = Ae^{-px}$, was fitted and it was found that $A = 213$ and $p = -0.808$, both found without errors. This law found to approximate the observed trend. For small values of N (e.g., $N \sim 1500$), the relative difference is relatively large. However, for $N > 2000$, the relative difference appears to plateau at approximately 1%. Whilst the fitted model does not capture the oscillatory features observed in the data, it provides a useful order-of-magnitude estimate for assessing the adequacy of the spatial resolution. In practice, this enables a quick diagnostic to determine whether the chosen step size is sufficiently small to yield physically meaningful results.

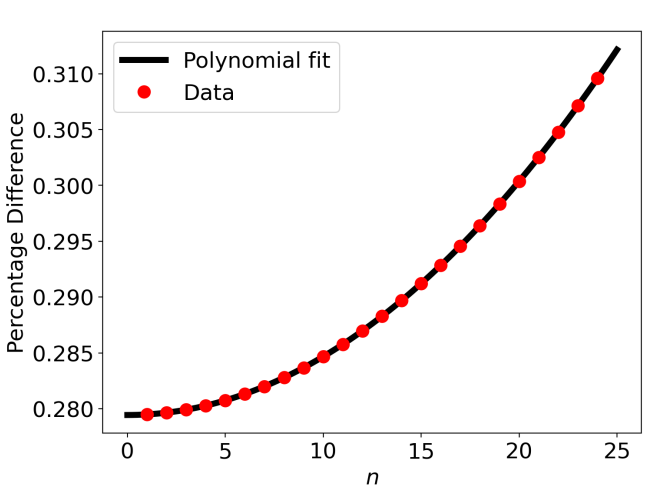

(a) Variation of the relative difference between E_{exp} and E_{calc} as a function of the principal quantum number, n, at $N = 5000$. The black line shows the polynomial fit applied to the raw data in red.

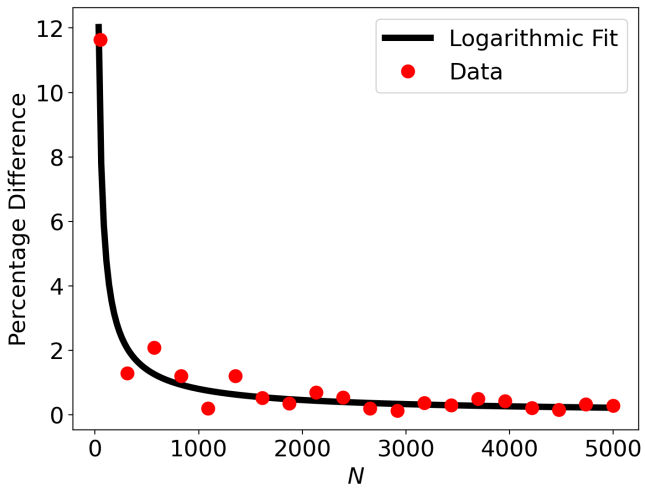

(b) Variation of the relative difference between E_{exp} and E_{calc} as a function of the number of spatial data points, N. The black line shows the polynomial fit applied to the raw data in red.

Figure 2: Comparison of how the relative difference between expected and calculated energies varies with (a) quantum number n, and (b) number of spatial data points N.

5.1.4 Testing the Harmonic Oscillator (Tom)

The solutions obtained when the finite difference method has been applied to the harmonic oscillator are shown below in **Figs. 3a, 3b**.

The numerical wavefunction solutions shown in **Fig. 3a** (coloured curves) are compared with the analytic solution (black dots). These are in excellent agreement and hold characteristic properties that you would expect for solutions of a simple harmonic oscillator system. These include: anti-symmetric solutions for odd n and symmetric solutions for even n. Futhermore each wavefunction obtained shows an exponential decay as x approaches $\pm\infty$ for all n which is consistent with the solutions discussed in the potentials section. **Fig. 3b** shows that at small n the calculated energy is in fantastic agreement with the expected energy. However, as the value of n increases, the relative difference the expected and calculated energies increases exponentially. This can be explained by the nature of the second order central difference approximation. As n increases, the magnitude of oscillations increases for each eigenstate. Consequently, the grid size becomes too large to resolve these rapid oscillations. This causes large errors in energy. This is a limitation of the finite difference method since smaller grid spacing requires more computational power.

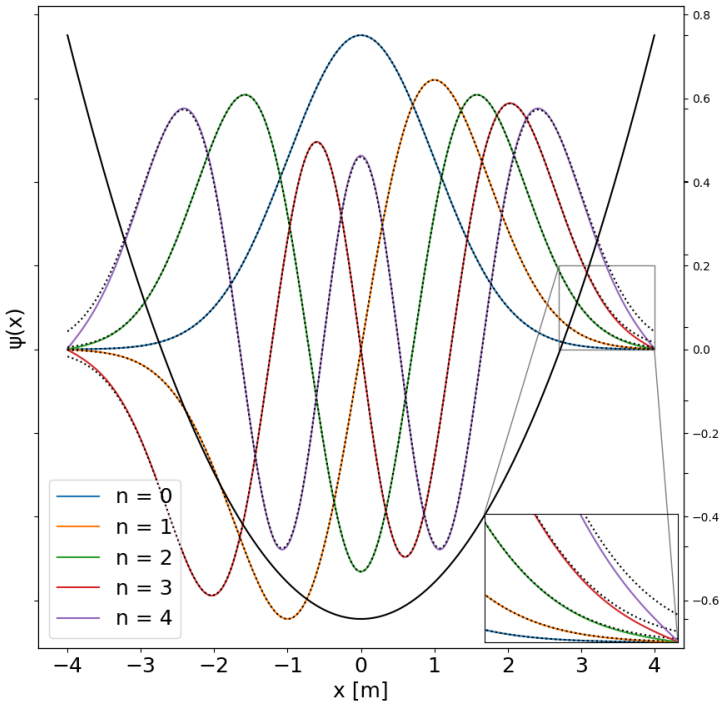

(a) Numerical solution obtained for simple harmonic oscillator. Dashed lines - Analytical solution. Coloured lines - Numerical solution

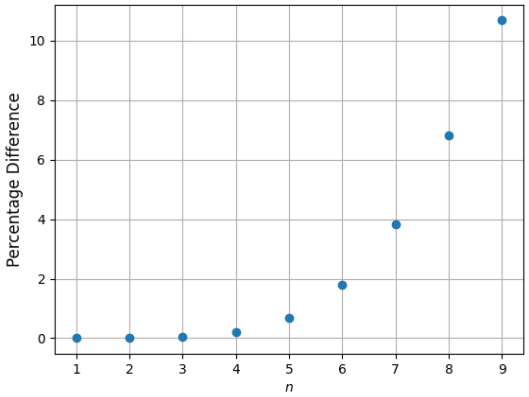

(b) Energy difference between expected and calculated energy levels for a harmonic oscillator as a function of n

Figure 3: Results obtained for the harmonic oscillator potential. The parameters used are: $m = 1, \omega = 1, \hbar = 1$

5.2 Crank–Nicolson Method (Jake)

5.2.1 Dispersion and Wave Packet Dynamics (Jake)

The Crank–Nicolson method was first tested by simulating a freely propagating quantum particle, corresponding to a vanishing potential ($V_0 = 0$). The initial condition was a Gaussian wave packet, expected to disperse as it evolved in time. As anticipated, the simulation showed the standard deviation of the packet increasing steadily, whilst the amplitude decreased in such a way that total probability was conserved.

This behaviour reflects a key feature of quantum mechanics, where a particle that is initially well localised in space must exhibit an inherent uncertainty in momentum, as described by the Heisenberg uncertainty principle. The broadening of the probability density over time arises because the individual momentum components of the wavefunction propagate at different speeds. The simulation correctly captured this de-localisation, offering a first validation of both the numerical scheme and its physical interpretation.

5.2.2 Boundary Effects and Norm Loss (Jake)

Further simulations investigated a wave packet with energy $E < V_0$ incident on a finite potential barrier of height $V_0 = 15$ (dimensionless units). The Crank–Nicolson scheme successfully reproduced the expected quantum tunnelling behaviour, with the packet partially transmitting through the barrier and partially reflecting, as illustrated in **Fig. 4**.

However, as the wave packet continued to evolve and approached the edges of the simulation domain, a loss in total probability was observed. This is most clearly seen in **Fig. 5**, where the wave packet reaches the right boundary and is partially reflected. A corresponding reduction in the norm of the wavefunction is plotted in **Fig. 6**, where the total norm falls from 1.0000 to approximately 0.9995. This loss is non-physical and arises because no boundary conditions or absorbing layers were implemented, meaning the wavefunction was effectively truncated as it left the domain. Although this effect seems minor, giving a $\sim 0.5\%$ decrease, the effects of multiple boundary reflections could add up and lead to numerical inaccuracy.

A simple solution would be to impose Dirichlet boundary conditions, for example enforcing $\psi(0,t) = \psi(L,t) = 0$ for all t. Whilst mathematically valid, this introduces artificial reflections that do not accurately represent open-boundary quantum systems. A more appropriate approach is to introduce a complex absorbing potential (CAP) that gradually damps the wavefunction near the boundaries without reflection. This is achieved by adding an imaginary potential of the form:

$$V_{\text{CAP}} = -i\alpha(x) \ , \tag{61}$$

where $\alpha(x)$ is a spatially varying absorption profile given by:

$$\alpha(x) = \begin{cases} A\left(1 - e^{-\frac{x-(x_{\min}+d)}{d}}\right), & \text{for } x < x_{\min} + d \\ A\left(1 - e^{-\frac{(x_{\max}-d)-x}{d}}\right), & \text{for } x > x_{\max} - d \\ 0, & \text{otherwise} \end{cases}, \tag{62}$$

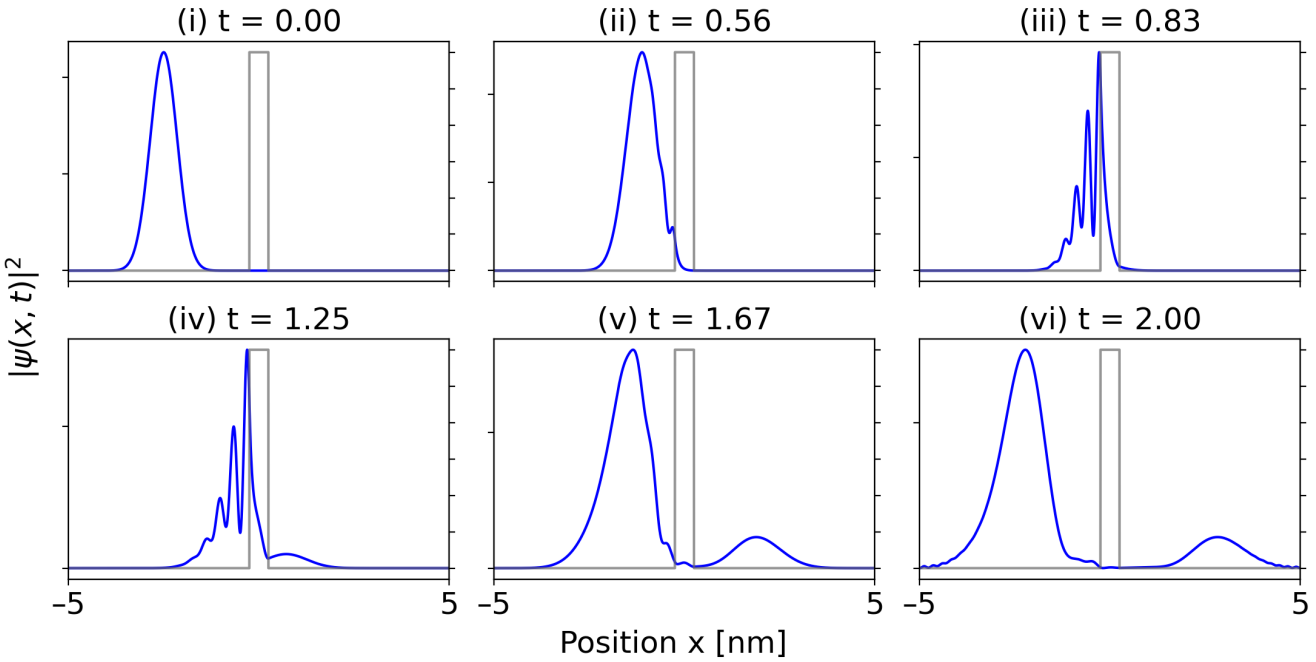

Figure 4: Time evolution of a Gaussian wave packet incident on a potential barrier of height $V_0 = 15$, being dimensionless and corresponding to $V_0 \approx 1.1$ eV, and has width $L = 1$. Each subplot corresponds to a different time step from $t = 0$ to $t = 2.00$, both being dimensionless times. The converted time that this simulation runs over is $t \approx 1.4$ fs. The initial Gaussian wave packet has parameters $v_g = 5$, $x_0 = 0$, $\sigma = 1$, with all of these being dimensionless. The wave packet undergoes partial transmission and reflection, characteristic of quantum tunnelling.

Here, A controls the strength of absorption, d defines the width of the damping layer, and $x_{\min}, x_{\max}$ are the spatial limits of the simulation domain. This approach, based on the method described by Jørgensen [4], provides a more physically accurate way to simulate open quantum systems.

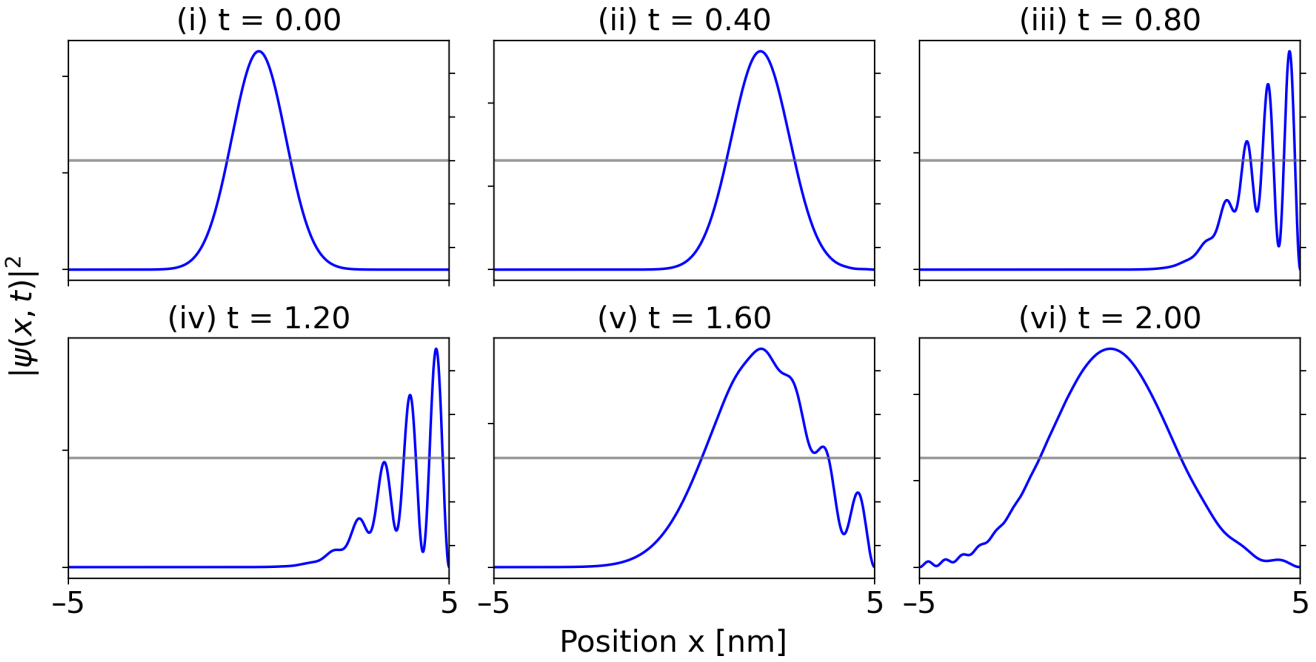

Figure 5: Snapshots showing the wave packet reaching the edge of the simulation domain. The lack of absorbing boundaries results in artificial reflection and probability loss. Each subplot corresponds to a different time step from $t = 0$ to $t = 2.00$, both being dimensionless times. The converted time that this simulation runs over is $t \approx 1.4$ fs. The initial Gaussian wave packet has parameters $v_g = 5$, $x_0 = 0$, $\sigma = 1$, with all of these being dimensionless.

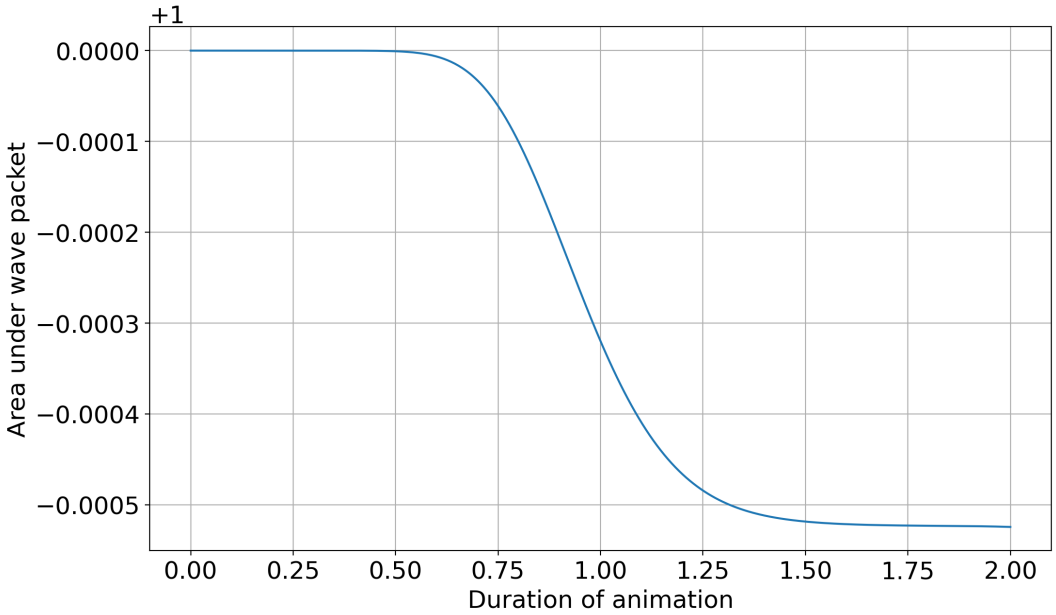

Figure 6: Reduction in the total norm of the wavefunction over time as the packet is truncated at the simulation boundary. Although the Crank–Nicolson method is theoretically norm-conserving, the absence of proper boundary conditions introduces artificial norm loss. The change is small (0.05%) but can accumulate due to repeated reflections at domain boundaries.

5.2.3 Time-Dependent Potentials and Framework Extensions (Jake)

A current limitation of the implementation is its restriction to time-independent potentials. At present, the potential $V(x)$ is evaluated once when the `Hamiltonian` object is initialised and stored as a fixed array. This prevents the simulation of systems where the potential evolves dynamically.

To address this, the potential should instead be re-evaluated at each time step within the `solve()` method. This would allow $V(x,t)$ to vary in time, opening the door to a much broader class of simulations. For full generality, the base `Potential` class would also need to be adapted to accept functions of both space and time.

Several physically relevant scenarios would then become accessible. One example is a quantum quench, where the potential is changed suddenly and drives the system out of equilibrium [31]. Another is a Floquet system, where the potential is periodically modulated in time, resulting in effective Hamiltonians with no static analogue [32]. These systems are widely studied in the context of ultracold atoms and driven condensed matter systems, and represent natural extensions of the current framework.

In the longer term, the same architecture could also be generalised to support higher-dimensional problems. For instance, two-dimensional wave packets or simplified atomic orbitals could be modelled, substantially broadening the range of physical systems that can be simulated.

5.3 Investigating Quantum Tunnelling (Toby, Tom, James)

To investigate the tunneling probabiltiy highlighted in **Eqn. 50**, two distinct simulations were conducted to investigate the exponential decay behaviour of an incoming wavevector incidient on a quantum well. Both a finite potential well and a double potential were investigated during the simulations. Each simulation varied a controllable parameter: the barrier width and the barrier height. To ensure the simulation captured meaningful trends, an appropriate range of parameter values was first established. This parameter space was efficiently explored using a Jupyter Notebook environment, which allowed for modular execution of code segments. This was particularly useful given the high computational cost of full simulations, which could take approximately 20 minutes to complete.

Initial setup involved visualizing the potential well and running a preliminary simulation to verify that the system behaved as expected. In accordance with the normalization procedure described in section 5.2.2, care was taken to select a simulation duration that would ensure both stability and consistency in the extraction of tunnelling coefficients. Upon this setup, each simulation was refined by adjusting grid spacing and time steps to ensure and accurate and stable computation - much similar to the consideration taken for simulation duration.

5.3.1 Barrier Widths

To investigate the effect barrier width had on the probability of quantum tunnelling occurring, the data was fitted to an exponential decay curve of the form:

$$Ae^{-bx} + c. \tag{63}$$

During the simulation a value of $E = 12.5\ eV$, $V_0 = 15\ eV$ and (using natural units) $m = \hbar = 1$. **Eqn. 50** therefore becomes:

$$\Omega = e^{-W\sqrt{20}}. \tag{64}$$

In order to compare the theoretical prediction, the simulated data, shown in **Figure:** 10a was fitted to an exponential, as highlighted in **Eqn. 63** using the curve fit function from `scipy`. This fit, shown in (**Figure.**10b), was found to be:

$$1.07e^{-3.08W} + 0.076. \tag{65}$$

As can be seen from **Eqn. 65**, the simulated data does conform perfectly to the theoretical model predicted by **Eqn. 50**. The tunnelling coefficient saturates to a non zero value of 0.076 as barrier width is increased to large values. This contrasts the theory which predicts a tunnelling coefficient of zero at large barrier widths. This difference could potentially be explained by the computational limitations of the simulation. As the number of grid points, N, increases, the precision of the Crank-Nicolson method also increases. During the simulations, the maximum number of grid points used the most that CoCalc would allow. To explain the difference between the simulation and the theory, further investigation would be required.

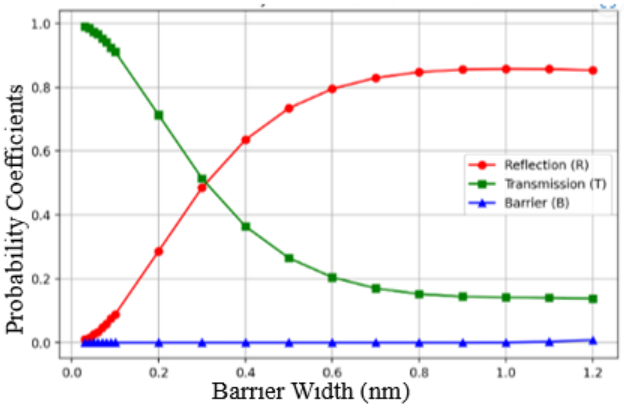

(a) The Reflection, Transmission coefficients at time ($t = 2$) as a function of barrier width.

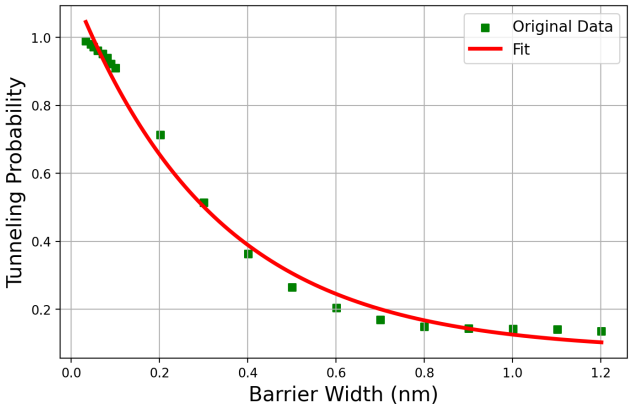

(b) TThe exponential fit of the Transmission coefficient modelled according to **Eqn. 50**.

Figure 7: The Quantum tunnelling coefficients as functions of barrier width (nm), (a) shows the raw data and trends followed by each whereas (b) fits the Transmission coefficient with an exponential decay curve with $Ae^{bx} + C$

5.3.2 Barrier Heights

To investigate the effect that barrier height has on the tunnelling probability, the previous values of $E = 12.5\ eV$ and $m = \hbar = 1$ remained unchanged, the barrier width was decided to be fixed at 1 nm. It was important to ensure the square root in the exponential of **Eqn. 50** did not turn complex. This means that the barrier height V_o has to be greater than the kinetic energy of the incident particle. Because of this constraint, the minimum barrier height was designated to be 13 eV. The energy range chosen was $(13 - 24)\ eV$. This approach however had an unexpected consequences. It was found that the tunnelling probability was extremely sensitive to adjustments in barrier height. This is shown in **Fig** 10a.

To test the simulated data, an exponential decay was again fitted and compared to the theoretical model. **Eqn. 50** becomes:

$$\Omega = e^{-(V_0 - E)\sqrt{8}}, \tag{66}$$

The simulated data yielded an exponential decay of:

$$0.58e^{-0.67(V_0 - E)} - 0.07. \tag{67}$$

The exponents in the exponentials differ by 421 %. This clearly doesn't satisfy the 3σ consistency criterion. To achieve better agreement, two modifications to the experimental approach can be implemented: either extending the measurement range to include additional barrier heights in the 12.5–13J interval, or decreasing the barrier width to produce a more gradual decay characteristic. The increased range would allow for sampling over the whole decay characteristic for a better fit. Decreasing the barrier width would decrease the exponent on **Eqn. 66** and thus make the exponential decay profile more gradual and more importantly more easily capturable by a plot. A limited number of attempts to do this were undertaken as a potential easy fix but this was not replicated on plots and is therefore an area of further investigation.

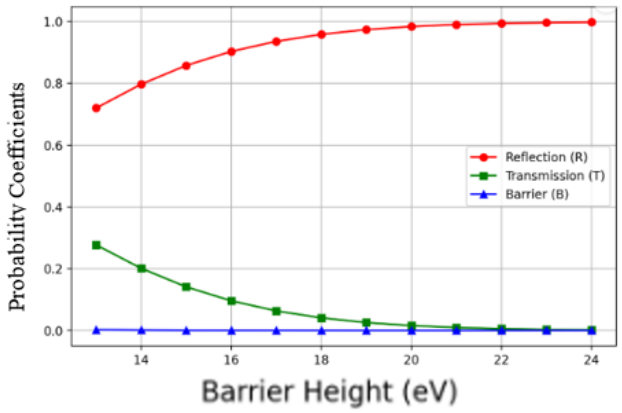

(a) The Reflection, Transmission coefficients at time ($t = 2$) as a function of barrier height.

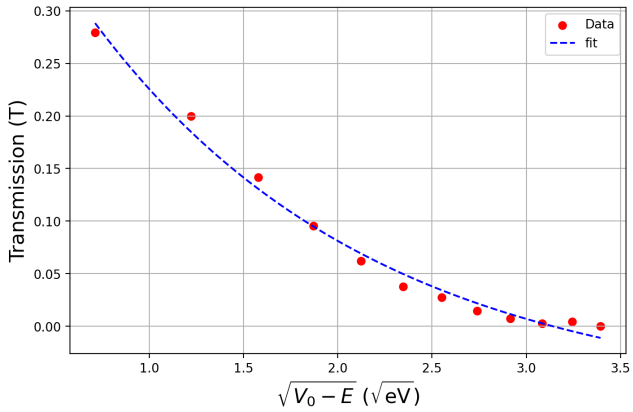

(b) The exponential fit of the Transmission coefficient modelled according to **Eqn. 50**.

Figure 8: The Quantum tunnelling coefficients as functions of barrier height, (a) shows the raw data and trends followed by each whereas (b) fits the Transmission coefficient with an exponential decay curve with $Ae^{bx} + C$.

5.4 Advanced Effects

This section explored some more nuanced effects where there is a limited amount of quantitative data and theory and this is reflected in the results and interpretations, what is confirmed is not a complete picture but just provides a small insight into some advanced effects when looking at tunnelling.

5.4.1 Double Potential well - Resonance

Quantum tunnelling was also investigated when a wave packet was incident on a double potential well. As previously discussed, the double potential well consisted of two finite potential wells, separated by a small distance ,b. The double potential well caused the observed tunnelling probability to oscillate as b increased. The addition of a double potential well allowed for more complex interference as the wave packet interacted with itself. When constructive interference occurred, the tunnelling probability dramatically increased and when destructive interference occurred, probability decreased.

Resonance effects on the transmission probability when an initial wave packet was propagated towards a double potential well can be shown below: As illustrated in **Fig. 9a**, a smooth resonant pattern emerges when the spacing between the two potential barriers is varied. The overall trend of exponential decay in transmission probability is preserved, as shown in **Fig. 9b**, where each resonant peak has been modelled individually as a discrete dataset.

Due to the complexity of the potential profile, there is no single, closed-form expression for the tunnelling coefficient in this double-well configuration. Consequently, the results in this section are primarily qualitative in nature.

Notably, the enhanced transmission at resonance highlights the non-trivial nature of quantum interference in double-well systems. If the system were treated as two independent single barriers, the expected trans-

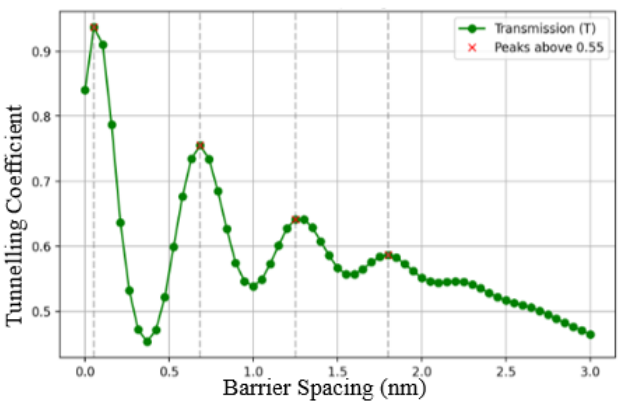

(a) The Reflection, Transmission coefficients at time ($t = 2$) as a function of the spacing between barriers in a double potential well

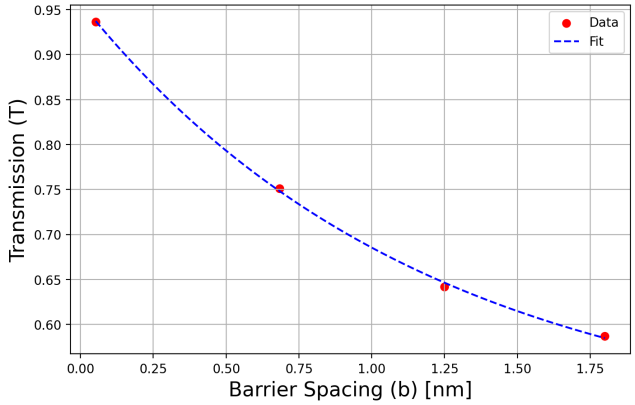

(b) An exponential fit of the resonant peaks for peaks above T = 0.55, this revealed some new information when looking at peak spacing and further verified exponential decay of T

Figure 9: An investigation into the quantum tunnelling effects onto a double potential well this causes an interference from the wave packet as it interferes with itself, a) Shows the tunnelling probability as a function of the spacing between the wells and b) shows an exponential fit of the resonant peaks

mission probability would be significantly lower. For reference, the potential wells in this configuration each have a width of 0.5 nm and a height of 25 eV. By comparison, in the single-barrier case shown in **Fig. 7b**, a barrier of width 1 nm and height 15 eV yields a transmission coefficient below 0.2. Yet, under resonant conditions in the double-well system, the transmission probability can exceed 0.9—even for stronger, narrower barriers—demonstrating the substantial role of interference in tunnelling enhancement.

5.4.2 Hartman effect

In this project the transmission time, τ_{trans} , was investigated as well as the dwell time, τ_{dwell}. For this investigation a simple finite potential well was chosen with the initial conditions of barrier height $V_0 = 25\ eV$ and initial wave packet velocity of 5 nm/s. The barrier width was varied between the range $(0.5 < W < 0.9)$ nm, the tunnelling times were calculated and extracted as a function of barrier width. In addition, the transmission time was compared against the barrier width to find an apparent tunnelling speed, the results can be seen below:

As can be seen above, for all of the values of barrier width, $\tau_{\text{transmission}}$ is greater than τ_{dwell}. This was not the initial expectation, however, since the time that the particle spends in the barrier should take up a large proportion of the simulation time of $t = 2$s. This result was a consequence of the barrier reflecting a meaningful amount of the wavefunction. This meant that a significant portion of the wave function did not spend any time within the barrier. This could be amended by considering a weaker less reflecting barrier, and on account of this, further analysis of dwell time was not necessary. The transmission time was propagated to calculate an apparent tunnelling velocity as a function of such barrier width seen. This can be seen in **Fig.10b**. This result also did match the initial expectation. The initial group velocity of the wave-packet was set be 5 nm/s, it was therefore an assumption that the tunnelling speed was also going to be constant. However, a complex relationship that appeared linear in shape initially and then

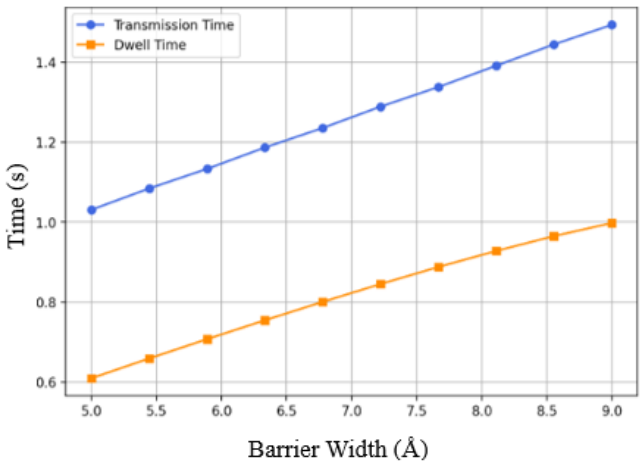

(a) Transmission time and dwell time as functions of barrier width for tunnelling through a finite potential well

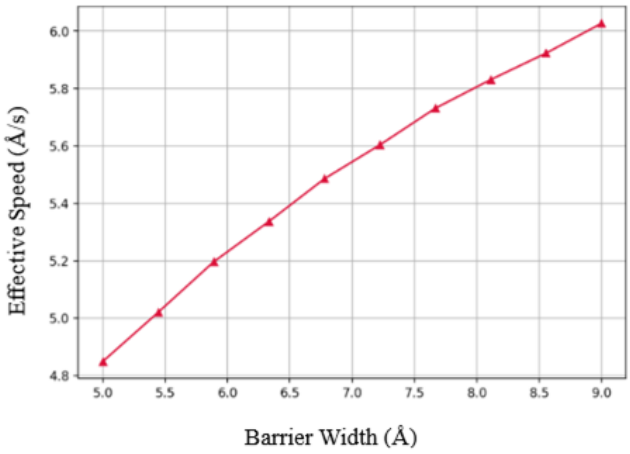

(b) The apparent tunnelling speed for the transmission time as a function of barrier width

Figure 10: The investigation into the time taken for a particle to tunnel, two popular interpretations, $\tau_{transmission}$ and τ_{dwell} were plotted against barrier width in a) and $\tau_{transmission}$ was propagated to plot an effective tunnelling speed as a function of barrier width seen in b)

plateaus towards greater barrier widths was returned. This phenomenon is referred to as the Hartman effect. The Hartman effect states that the tunnelling time becomes independent of barrier length for thick enough barriers, ultimately resulting in unbounded tunnelling velocities. Experiments done with "single photons", classical light waves, and microwaves all show this apparent superluminality [33]. In fact, experiments with "single photons" [34], classical light waves [35], and microwaves [36] all observe apparent super-luminality when calculating the velocity as

$$v_{\text{apparent}} = \frac{w}{\tau_{\text{transmission}}}. \tag{68}$$

However, this interpretation is misleading—while the formula holds mathematically, it relies on the classical assumption that τ represents a well-defined transit time through the barrier. Quantum mechanics forbids this interpretation in classically forbidden regions, where no single trajectory exists.

The resolution lies in recognizing that the particle follows all causally accessible paths, which interfere destructively and constructively. Path summation methods [37] properly account for this quantum behaviour, showing that v_{apparent} emerges from wave interference rather than genuine faster-than-light propagation. Crucially, even after this correction, the calculated v_{apparent} may still exceed c, but this does not imply superluminal information transfer or a violation of relativity. Instead, it reflects the inadequacy of applying classical trajectory-based concepts to quantum tunnelling phenomena.

5.5 Radial Eigenfunctions (Jake)

5.5.1 Implementation (Jake)

Following the implementation of the `RadialHamiltonian` class, with the necessary modifications to the potential definition as described earlier, the final results were obtained and are shown in **Fig. 11**. The calculated radial wave-functions display good overall agreement with those generated analytically using `sympy.physics.hydrogen.R_nl()`, though slight discrepancies can be observed across some eigenstates.

One likely contributor to these differences is the choice of spatial resolution, set to $N = 5000$ points. While this was sufficient to produce smooth and physically meaningful results, attempts to increase the resolution beyond this value led to issues with computational performance. In particular, higher resolutions resulted in significantly longer runtimes and, in some cases, caused the program to crash due to insufficient memory resources. This limitation highlights the trade-off between numerical precision and computational feasibility when solving the radial Schrödinger equation using dense grids.

A natural extension of this work would be to incorporate the angular components of the wave-function, allowing the full solution $\psi_{n\ell m}(r, \theta, \phi) = R_{nl}(r)Y_l^{m_l}(\theta, \phi)$ to be reconstructed. Alternatively, the framework could be generalised to approximate multi-electron systems such as helium, which would involve modifying the potential to account for electron–electron interactions and applying appropriate approximations to maintain tractability.

5.5.2 Verifying Radial Eigenfunctions (Jake, James)

To verify the accuracy of the computed radial eigenfunctions, two approaches were taken. The first involved a direct comparison between the numerically obtained eigenfunctions and their corresponding analytical forms. The results are presented in **Fig. 11**. Although the data points are not perfectly aligned due to the finite grid resolution used in the numerical method, the agreement is remarkably close. The numerically calculated radial probability densities clearly follow the expected trends of the analytical solutions, with all key features—such as node positions and asymptotic behaviour—well captured.

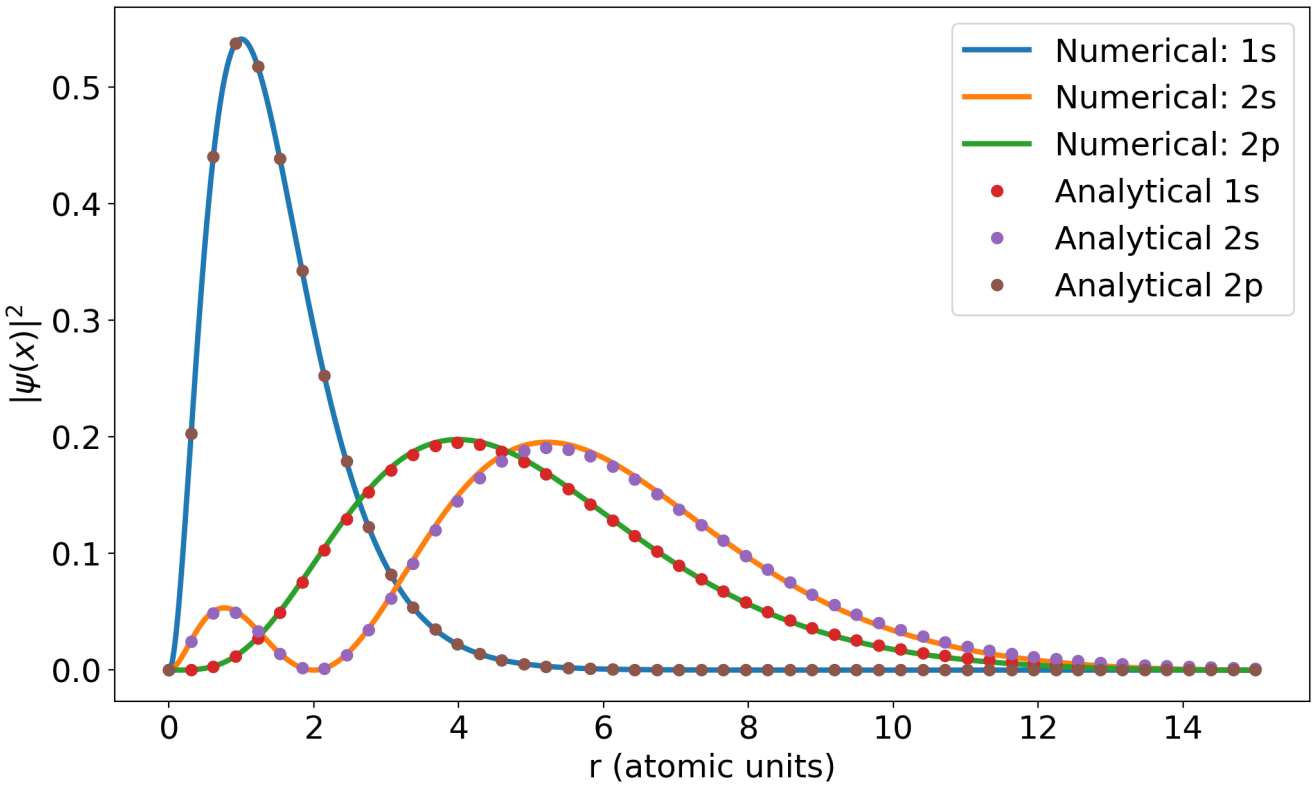

Figure 11: Radial probability densities plotted against radius in atomic units. The numerically obtained solutions for the 1s (blue), 2s (orange), and 2p (green) states are shown as solid lines, while the corresponding analytical solutions for 1s (red), 2s (purple), and 2p (brown) are shown as discrete markers. Excellent agreement is observed across all states, with minor discrepancies attributable to numerical resolution limits.

The second method of validation focused on comparing the energy eigenvalues produced by the numerical solver with the known analytical results. According to **Eqn. 49**, the energy levels of the hydrogen atom depend only on the principal quantum number n, and not on the orbital angular momentum ℓ. As a result, the 1s state is expected to have an energy of $E_1 = -13.6$ eV, while the 2s and 2p states should be degenerate with $E_2 = -3.4$ eV.

The numerical eigenvalues were found to be in excellent agreement with these theoretical predictions. The ground state (1s) energy was calculated as $E_1 = -13.55$ eV, while the 2s and 2p states yielded energies of $E_2 = -3.37$ eV and $E_2 = -3.38$ eV, respectively. These small deviations from the exact values are consistent with the level of discretisation used in the radial grid and further support the accuracy of the numerical implementation.

6 Conclusion

The finite difference method was successfully applied to the time-independent Schrödinger equation by discretising the continuous derivatives onto a spatial grid of N points with uniform spacing Δx. This allowed for the numerical computation of energy eigenvalues and eigenfunctions for a given potential, found to form an orthonormal set, with results found to lie within 0.5% of the expected analytical values, provided an appropriate choice of N was made.

Building on the successful implementation of the finite difference method, the solver was extended to model the time-dependent Schrödinger equation using the Crank–Nicolson scheme, which is both norm-preserving and second-order accurate. This allowed for the simulation of a freely propagating wave packet, with the observed dispersion behaviour consistent with predictions from the Heisenberg uncertainty principle. The accompanying animation tool proved highly effective in visualising the evolution of the wave-function over time, providing clear insight into the system's dynamics. A minor numerical issue was observed when the wave-function reached the edge of the simulation domain, leading to a small reduction in norm due to artificial reflection. This could be resolved in future work by implementing a complex absorbing potential at the boundaries. A further limitation of the current framework is its restriction to time-independent potentials. However, with relatively minor modifications, the code could be adapted to support fully time-dependent scenarios.

The numerical framework developed gave an opportunity to explore quantum tunnelling, where a wave packet propagates through a classically forbidden potential barrier. By adapting the existing solver to include a static potential barrier, the same Crank-Nicolson scheme could be used to simulate tunnelling probabilities as a function of barrier height, width and the initial wave packet velocity. The measured transmission was then compared to the theoretical value to establish efficiency of the model. Building on this, the unique phenomenon of quantum tunnelling through a double potential well gives rise to interference effects, resulting in a resonant transmission profile. The complex dynamics of particle tunnelling time were investigated, revealing a relationship between apparent tunnelling velocity and barrier width that gives rise to the Hartman effect—where the effective tunnelling time becomes independent of barrier width beyond a certain threshold.

Upon completion of the time-dependent solver, the framework was further extended to compute the radial eigenfunctions of the hydrogen atom. This involved incorporating the effective potential arising from the electron's orbital angular momentum, enabling the correct treatment of different ℓ-states. The implementation was highly successful, with the computed eigenvalues and eigenfunctions showing excellent agreement with the known analytical solutions for hydrogenic atoms. This extension demonstrates the flexibility of the numerical approach and provides a strong foundation for more advanced models. In particular, the framework could be expanded to include the full three-dimensional hydrogen wave-function by incorporating the angular components.

7 Bibliography

References

[1] Erwin Schrödinger. Quantization as an eigenvalue problem. I. *Annalen der Physik*, 79(4):361–376, 1926. Original German title: Quantisierung als Eigenwertproblem. I.

[2] R. D. Richtmyer and K. W. Morton. *Difference Methods for Initial-Value Problems*. Interscience Publishers, New York, 1967.

[3] J. Crank and P. Nicholson. A practical method for numerical evaluation of solutions of partial differential equations of the heat-conduction type. *Proceedings of the Cambridge Philosophical Society*, 43(1):50–67, 1947.

[4] Loren Jørgensen, David Lopes Cardozo, and Etienne Thibierge. Numerical resolution of the schrödinger equation. Technical report, École Normale Supérieure de Lyon, Master Sciences de la Matière, 2011. Available online: `https://web.pa.msu.edu/people/duxbury/courses/phy480/SchrodingerDynamics.pdf`.

[5] Charles H. Townes and Arthur L. Schawlow. *Microwave Spectroscopy*. McGraw-Hill, 1955. Includes discussion of the ammonia inversion spectrum and its use in molecular spectroscopy.

[6] Britanica L. Pearce Williams. Science and the industrial revolution. `https://www.britannica.com/science/history-of-science/Science-and-the-Industrial-Revolution`. Accessed: 28/04/2025.

[7] Insitute of physics. Maxwell's equations what's the foundation of modern technology? `https://www.iop.org/explore-physics/big-ideas-physics/maxwells-equations`. Accessed: 28/04/2025.

[8] Rob Hudson. James jeans and radiation theory. *Studies in History and Philosophy of Science Part A*, 20(1):57–76, 1989.

[9] The Physics Hypertextbook. Black body radiation. `https://physics.info/planck/#:~:text=Planck's%20law%20is%20a%20formula,angle%20per%20area%20per%20wavelength.` Accessed: 28/04/2025.

[10] Stephen Klassen. The photoelectric effect: Reconstructing the story for the physics classroom. *Science & Education*, 20:719–731, 2011.

[11] Helge Kragh. *Niels Bohr and the quantum atom: The Bohr model of atomic structure 1913-1925*. Oxford University Press, 2012.

[12] Claude Elbaz et al. Wave-particle duality in einstein-de broglie programs. *Journal of Modern Physics*, 5(18):2192, 2014.

[13] Libretexts physics. Lectu time-dependent schrödinger equation. `https://phys.libretexts.org/Bookshelves/Nuclear_and_Particle_Physics/Introduction_to_Applied_Nuclear_Physics_(Cappellaro)/06%3A_Time_Evolution_in_Quantum_Mechanics/6.01%3A_Time-dependent_Schrodinger_equation`. Accessed: 29/04/2025.

[14] DM Causon and CG Mingham. *Introductory finite difference methods for PDEs*. Bookboon, 2010.

[15] Gerald W Recktenwald. Finite-difference approximations to the heat equation. *Mechanical Engineering*, 10(01), 2004.

[16] A. Yew. Numerical differentiation: finite differences. `https://www.dam.brown.edu/people/alcyew/handouts/numdiff.pdf`. Accessed: 28/04/2025.

[17] Scipy. `https://docs.scipy.org/doc/scipy/reference/generated/scipy.linalg.eigh_tridiagonal.html`. Accessed: 29/04/2025.

[18] Tyler Chen. The lanczos algorithm for matrix functions: a handbook for scientists, 2024.

[19] T. C. Sharma, S. P. Pathak, and G. Trivedi. Comparative study of crank-nicolson and modified crank-nicolson numerical methods to solve linear partial differential equations. *Indian Journal of Science and Technology*, 17(10):924–931, 2024.

[20] Dr. Dan Protopopescu. Potential well. `https://www.ppe.gla.ac.uk/~protopop/teaching/QUM/L13-QUM-2012h.pdf`. Accessed: 29/04/2025.

[21] University of Liverpool Bradley cheal. Phys361, lecture 5a. `https://canvas.liverpool.ac.uk/courses/77589/pages/weeks-4-6-potentials`.

[22] V. Jelic and Edmonton F. Marsiglio Department of Physics, University of Alberta. The double well potential in quantum mechanics: a simple, numerically exact formulation. `https://ar5iv.labs.arxiv.org/html/1209.2521#:~:text=The%20double%20well%20potential%20is,important%20in%20quantum%20information%20theory.`

[23] Libre Texts Physics. Harmonic oscillator- brute force approach. `https://phys.libretexts.org/Bookshelves/Quantum_Mechanics/Essential_Graduate_Physics_-_Quantum_Mechanics_(Likharev)/02%3A_1D_Wave_Mechanics/2.10%3A_Harmonic_Oscillator-_Brute_Force_Approach`. Accessed: 26/04/2025.

[24] Rachel Dudik. The quantum harmonic oscillator. `http://physics.gmu.edu/~dmaria/590%20Web%20Page/public_html/qm_topics/harmonic/`. Accessed: 28/04/2025.

[25] Luca Nanni. The hydrogen atom: A review on the birth of modern quantum mechanics. *arXiv preprint arXiv:1501.05894*, 2015.

[26] The University of Edinburgh. Lecture 10 - central potential. `https://www2.ph.ed.ac.uk/~ldeldebb/docs/QM/lect10.pdf`. Accessed: 28/04/2025.

[27] RADIOACTIVITY.EU.COM. decay : tunnel effect. `https://radioactivity.eu.com/articles/phenomenon/tunnel_effect`. Accessed: 26/04/2025.

[28] TJ Vink, KJBM Nieuwesteeg, and G Oversluizen. Tunneling through thin oxide interface layers in a-si: H schottky diodes. *Journal of applied physics*, 71(9):4399–4404, 1992.

[29] Mohsen Razavy. *Quantum theory of tunneling*. World Scientific, 2013.

[30] Pauli Virtanen, Ralf Gommers, Travis E. Oliphant, Matt Haberland, Tyler Reddy, David Cournapeau, Evgeni Burovski, Pearu Peterson, Warren Weckesser, Jonathan Bright, Stéfan J. van der Walt, Matthew Brett, Joshua Wilson, K. Jarrod Millman, Nikolay Mayorov, Andrew R. J. Nelson, Eric Jones, Robert Kern, Eric Larson, C J Carey, İlhan Polat, Yu Feng, Eric W. Moore, Jake VanderPlas, Denis Laxalde, Josef Perktold, Robert Cimrman, Ian Henriksen, E. A. Quintero, Charles R. Harris, Anne M. Archibald, Antônio H. Ribeiro, Fabian Pedregosa, Paul van Mulbregt, and SciPy 1.0 Contributors. SciPy 1.0: Fundamental Algorithms for Scientific Computing in Python. *Nature Methods*, 17:261–272, 2020.

[31] M. A. Cazalilla and M. Rigol. Focus on dynamics and thermalization in isolated quantum many-body systems. *New Journal of Physics*, 12(5):055006, 2010.

[32] André Eckardt. Colloquium: Atomic quantum gases in periodically driven optical lattices. *Reviews of Modern Physics*, 89(1):011004, 2017.

[33] Herbert G. Winful. Tunneling time, the hartman effect, and superluminality: A proposed resolution of an old paradox. *Physics Reports*, 436(1–2):1–69, 2006.

[34] Raymond Y. Chiao and Aephraim M. Steinberg. Vi: Tunneling times and superluminality. *Progress in Optics*, 37:345–405, 1997.

[35] A. Enders and G. Nimtz. On superluminal barrier traversal. *Journal de Physique I*, 2(9):1693–1698, 1992.

[36] M. Büttiker and S. Washburn. Ado about nothing much? *Nature*, 422:271–272, 2003. Commentary/opinion piece.

[37] Yun-ping Wang and Dian-lin Zhang. Reshaping, path uncertainty, and superluminal traveling. *Physical Review A*, 52(4):2597–2600, October 1995.

A Individual Contributions

A.1 Jake Libbeter

I played a key role in the group, contributing substantially to both the coding and implementation phases of the project. In particular, I was responsible for writing the code to discretise the Schrödinger equation and to solve the resulting eigenvalue problem, as described in **Eqn. 15**. I also implemented the Crank–Nicolson method for the time-dependent Schrödinger equation and developed the animation tool used to visualise wavefunction evolution. Whilst the underlying theory for these components was discussed collaboratively, the final implementation was primarily completed by me. The theory behind the extension to compute the radial eigenfunctions of the hydrogen atom was discussed with James, although the numerical code was again written predominantly by me. Overall, I believe the contributions across the group were well balanced, with each member investing significant effort either in the theoretical analysis or the practical implementation.

A.2 James Freeman

My role in the project mainly evolved researching theory and discussing this with group members as well as implementing aspects of the potentials class and aiding in the investigation into quantum tunnelling. This included investigating the finite difference and Crank-Nicholson method (alongside Toby). This included being able to present the theory for a report and discuss with Jake what was needed for the code. Also, I worked on studying the quantum wells we could use the project. This included working with Tom to implement a potentials class which was successful in being used to solve the Schrödinger equation. As well as this I worked on the initial concepts of trying to calculate the Transmission and reflection coefficients. This was initially a challenging problem as is the incident and reflected waves were unseperable in terms of the code. I spent considerable time on this problem with Toby in for us to be able to Calculate the Incident, Reflection, Barrier and Transmission coefficients. I also discussed the theory behind the radial Schrodinger equation with the group and what the possibility of investigation was in this area. This ultimately led to Jake implementing the code behind this. Following this, I turned my attention to the report, initially formatting the introduction and making progress on describing the theory of the project, whilst others were finalising the analysis.

Overall, I feel the group has worked very well together. There has been very good communication between all members discussing what has been done and what further investigation could be conducted. I feel this has ensured all group members have contributed equally to this project.

A.3 Toby Brown

My role in the project evolved over time, beginning with research-focused tasks such as investigating the finite-difference method for discretizing the Schrödinger equation and the Crank-Nicolson scheme for the time-dependent case. This work contributed to the foundational framework of the report before transitioning to more technical implementation.

After Jake developed the animation tool and Tom/James established the potentials class, I shifted focus to coding and analyzing quantum tunneling phenomena. This included modeling transmission probabilities

for key parameters (barrier width and height) and comparing results with theoretical predictions. I further explored resonant tunneling effects in double potential wells and investigated the concept of tunneling time, including its dependence on barrier properties.

Collaboration and communication were critical to our team's success. Regular discussions of ideas and theories expanded the project's scope greatly beyond initial expectations, ensuring balanced contributions across all members.

A.4 Thomas Bickley

My role within this project started out with investigating different quantum potentials and their solutions to the Schrodinger equation alongside James - This was very important to compare numerical vs analytic solutions. Next we implemented potential classes within python which were a critical component to be used for the finite difference and crank-nicolson method that Jake had developed. Once the finite difference method was complete, comparisons between our numerical and analytical results were drawn in the form of plots.

After this, i helped out Toby and James with analysing quantum tunnelling, we started out by researching transmission coefficients and subsequently how to obtain them from our simulations. These coefficients would then form a basis to find even more results within our investigation.

Overall, i felt that we as a group worked exceptionally throughout this project. Everyone provided consistent and valuable input. This was paired with excellent communication, allowing us to stay well co-ordinated and make consistent and steady progress. It was a pleasure working with this group